ELSEVIER

Journal of Nuclear Materials 244 (1997) 85–100

journal of nuclear materials

RACLETTE: a model for evaluating the thermal response of plasma facing components to slow high power plasma transients. Part I: Theory and description of model capabilities

A. René Raffray *, Gianfranco Federici

ITER Garching JWS, c / o Max-Planck-Institut für Plasmaphysik, Boltzmannstr. 2, D-85748 Garching, Germany

Received 10 May 1996; accepted 16 September 1996

Abstract

RACLETTE (Rate Analysis Code for pLasma Energy Transfer Transient Evaluation), a comprehensive but relatively simple and versatile model, was developed to help in the design analysis of plasma facing components (PFCs) under 'slow' high power transients, such as those associated with plasma vertical displacement events. The model includes all the key surface heat transfer processes such as evaporation, melting, and radiation, and their interaction with the PFC block thermal response and the coolant behaviour. This paper represents part I of two sister and complementary papers. It covers the model description, calibration and validation, and presents a number of parametric analyses shedding light on and identifying trends in the PFC armour block response to high plasma energy deposition transients. Parameters investigated include the plasma energy density and deposition time, the armour thickness and the presence of vapour shielding effects. Part II of the paper focuses on specific design analyses of ITER plasma facing components (divertor, limiter, primary first wall and baffle), including improvements in the thermal-hydraulic modeling required for better understanding the consequences of high energy deposition transients in particular for the ITER limiter case.

1. Introduction

Plasma facing components (PFCs) in the next-step fusion devices are subject to high quasi steady-state heat loads during operation. In addition, they have to accommodate peak transient energy deposition resulting from off-normal plasma conditions. Short term plasma disruptions depositing energy on PFCs over $\simeq$ 1–10 ms results in loss of armour material through vaporisation and melting (in the case of metal armour) but with little effect on the heat flux through the armour/substrate interface to the coolant whose time constant is much higher. Off-normal plasma behaviour can also lead to high transient energy deposition on PFCs over longer time scales. For example, in the current engineering design phase of the International Thermonuclear Experimental Reactor (ITER), it is anticipated that plasma vertical displacement events (VDEs) could occur during operation resulting in plasma energy deposition of $\simeq$ 10–100 MJ/m^2 over 0.1–1 s onto part of the PFC surface [1]. These 'slow' transient events would also result in substantial armour vaporisation and melting (for metal armour) whose extent depends on the energy density and deposition time; in addition, since the energy deposition time scale is of the order of the armour thermal diffusivity time constant, large heat fluxes could result through the armour/heat sink interface to the coolant.

To help understand the consequences of these events on the armour, quite sophisticated models have been developed. These models have tended to address the fast transient resulting from plasma disruptions, thus focusing on the plasma/armour interface including gas dynamics modeling of the vapourised armour, without coupling the PFC block thermal response and coolant behaviour. Refs. [2–7] describe good examples of such models and of their application to fast disruption analysis.

In most of these models, three major plasma/material

* Corresponding author. Tel.: +49-89 3299 4406; fax: +49-89 3299 4163; e-mail: raffrar@sat.ipp-garching.mpg.de.

PII S0022-3115(96)00680-0

interaction phenomena are included. First, the thermal and material response against the initial burst of energy delivered to the PFC is analysed by considering the particle and heat deposition and the material thermal evolution including phase-changes, moving boundaries, and temperature dependent thermophysical properties. Second, as a result of the sudden ablation, a vapour cloud is formed in front of the incoming plasma particles and one has to solve the complex hydrodynamics and heating problem of the vapour cloud including effects of ionisation, excitation and photon radiation that shields the original surface. In this case to simulate as close as possible the conditions expected in fusion devices, the detailed effects of the magnetic field on the magnetohydrodynamics of the vapour cloud and on the resulting erosion rate (including effects such as magnetic field diffusion, friction forces, and Joule heating of the vapour material, sometimes in two-dimensional (2D) geometry) are also included in some of the most sophisticated computer codes (see, for example, Ref. [6]). Finally, to evaluate the net heat flux transmitted to the plasma facing materials, these models include radiation transport throughout the vapour clouds.

An area, where little modelling development exists, in spite of the strong implications expected on the design, concerns loss of melt layers developed in metals exposed to high disruption heat loads. Mechanisms which can contribute to melt layer loss are only partially understood and include effects such as melt splashing due to formation and boiling of volume bubbles that may result from continuous heating and overheating of the liquid layer during disruptions. Additionally, growth of hydrodynamic instabilities (e.g., Rayleigh–Taylor instabilities) in the melt layer subject to external forces (magnetic, gravity, vapour recoil forces) will affect the dynamics of the melt-layer evolution during a disruption and will determine the extent of the melt loss. Rather crude models to study-layer erosion are implemented in the model described in Ref. [7].

Other models have looked at the transient thermal behaviour of the PFC block including the coolant behaviour under high heat fluxes but without fully considering vaporisation, melting and possible vapour shielding effects. For example, in Ref. [8], the first wall of a fusion blanket is approximated by a slab, with the surface facing the plasma subject to an applied heat flux, while the rear surface is convectively cooled. The relevant parameters affecting the heat transfer during the early phases of heating as well as for large times are established. Analytical solutions for the temperature variation with time and space are derived. Other examples of thermal-hydraulic models for the first wall are given in Ref. [9] for cases including thermal mass barrier, tubular shield, and radiating liner.

Recently, a two-dimensional PFC block transient thermal model was developed focusing on the surface effects of 'slow' high power transients for given coolant conditions [10]. The model uses the ANSYS code [11] whereby surface melting is accounted through the change of the armour material enthalpy. The surface heat flux is set as a function of the surface temperature from a separately derived expression to account for evaporation, black body radiation and possible vapour shielding effects. Initial results from the model are interesting, including an assessment of the extent of Be armour melting under different conditions. However, the use of the model is quite tedious and, due in part to the very fine mesh required for solution in the PFC surface region, requires substantial computing time. It seems to be best used for specific well-identified runs, for example for calculations to confirm PFC behaviour in the final design stage or for calibration purposes.

The objective here was to develop a comprehensive but relatively simple and versatile model that could be used quickly and conveniently to help in the design analysis of plasma facing component under 'slow' transient plasma energy deposition but which would include all the key heat transfer surface processes such as evaporation, melting, and radiation, and their interaction with the PFC block thermal response and the evolving coolant conditions. This objective influenced the code development and, wherever possible, solutions that would help avoid cumbersome and lengthy procedures such as frequent iterations were adopted provided they did not significantly influence the outcome. In other words, given the status of knowledge of PFC thermal response and the uncertainties in defining the level of deposited plasma energy, a small loss of accuracy in the computations was deemed acceptable if it did result in a substantially simpler and faster code.

The model is called RACLETTE for Rate Analysis Code for pLasma Energy Transfer Transient Evaluation. To do justice to the breadth of the subject and to the range of analyses of particular relevance for ITER PFC design, it was decided to present the work in two sister and complimentary papers. The first paper here deals with model description, calibration and validation, and with a number of parametric analyses shedding light on and identifying trends in the PFC armour block response to high energy deposition transients. The second paper [12] focuses on specific design analyses of ITER PFCs (divertor, limiter, primary first wall and baffle), including improvements in the thermal-hydraulic modelling required for better understanding the consequences of high energy deposition transients in particular for the ITER limiter case.

This paper proceeds with a description of the model. Model calibration and validation are then discussed based on comparison with experimental and multi-dimensional computational results. Next, the capabilities of the model are illustrated through the presentation of a number of parametric studies from which responses of PFCs with various armour thicknesses to different energy deposition transients are discussed. Finally, key findings from the studies are summarised, and recommendations on future effort are proposed.

2. Model description

The objective was to develop a simple-to-use model but with capabilities to account for all the key heat transfer and erosion processes, as summarised in Table 1. The model is based on a simple one-dimensional (1D) geometry in keeping with objective of simplication wherever no significant loss in accuracy would result. As illustrated in Fig. 1, the model considers a unit-cell cross-section of a PFCincluding up to three material layers. For example, it could represent a primary first wall configuration of a thin stainless steel channel embedded in a copper matrix on top of which is attached a plasma-facing beryllium layer as armour. To account for two-dimensional effects in the case of a circular cooling channel, a correction factor is introduced to calculate the heat flux through the channel walls and to the coolant. The model considers the effects of evaporation, radiation and melting. In this version of the code, vapour shielding effects are not directly included. Instead, the plasma heat flux is included as a function of surface temperature based on separately computed vapour shielding results.

The model is based on the solution of the following transient heat conduction equation using an implicit finite difference scheme with a matrix solver, coupled with the energy balance equations at the surface, which provide boundary conditions for the solution:

$$\rho C_p \frac{\partial T}{\partial t} = \frac{\partial}{\partial x}\left(k\frac{\partial T}{\partial x}\right) + q'''(x,t), \tag{1}$$

where ρ, C_p and k are the temperature-dependent material density, specific heat and thermal conductivity respectively, x is the distance through the armour block and q''' is the volumetric heat generation.

The boundary conditions at the surface depends on whether the armour melting point has been reached (in case of metal armour) while the boundary conditions on the coolant side depends on whether subcooled boiling has been reached. These are described in details in the following subsections.

2.1. Surface boundary condition

For non-metal armour, and for metal armour, if the melting point of the armour has not been reached at the surface, the boundary condition is set using

$$-k\left(\frac{\partial T}{\partial x}\right)_{\text{surface}} = q''_{\text{pl}} - q''_{\text{rad}} - q''_{\text{evap}}, \tag{2}$$

where q''_{pl} is the net incoming plasma heat flux and q''_{rad}

Table 1
RACLETTE (Rate Analysis Code for pLasma Energy Transfer Transient Evaluation): Summary of mechanisms, features and capabilities

Mechanisms	Features/capabilities
· Surface processes (plasma side)	*all processes are a function of surface temperature; clamping of solid surface temperature at melting point; melt layer decoupled from PFC block to solve for surface temperature at each time step*
– evaporation	erosion and armour thickness evaluated at each time step
– change of phase/melting (for metals)	partial or total melt layer loss can be incorporated at each time step and armour thickness adjusted accordingly
– heat conduction through the melt layer	
– surface thermal radiation	to other cold PFC regions
– vapour shielding (plasma-flux attenuation)	based on separate calculations using the model discussed in Ref. [21]. For cases with vapour shielding incident power is given in input as a function of surface temperature
· Bulk processes	*solution of transient heat conduction equation with evolving boundary dimension and conditions*
– heat conduction	includes temperature dependence of material properties. (Also, for C-based material includes effect on thermal conductivity resulting from n-irradiation.)
– temperature levels and gradients	history through PFC block including all interfaces
– thermal stress/displacements	not included in initial model; heat flux used as a relative measure
– convection at the coolant side	
· Coolant behaviour	*simplified solution scheme for heat transfer in subcooled boiling regime based on minimisation of cumbersome iterations*
– heat transfer	detailed estimate of heat transfer for single-phase and sub cooled boiling regime 2D factor used to model 2D PFC block geometries reasonably well footprint factor used in estimating total heat flow to coolant to account for plasma energy density profile over channel length
– temperature	outlet temperature evaluated at each time step based on history of the heat flow to the coolant.
– critical heat flux conditions (CHF)	to be added, see part II of this paper [12]
– pressure drop	adjustment of coolant pressure for CHF estimate based on pressure drop calculation at each time step (to be added, see part II of this paper [12])

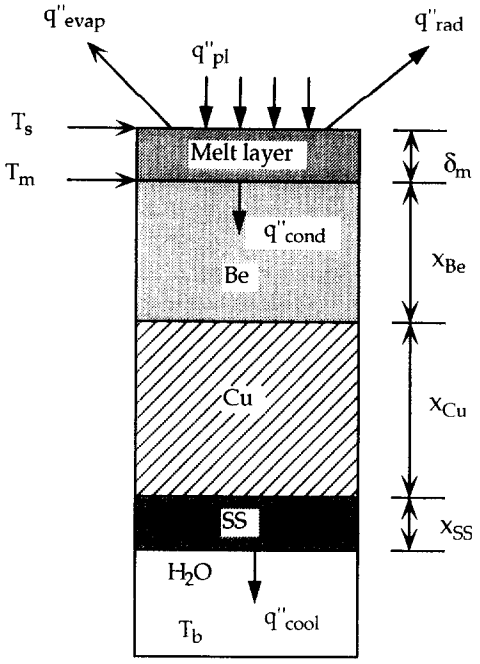

Fig. 1. Simple conduction model for transient analysis of plasma energy deposition on plasma facing surface including effect of melt layer, evaporation and radiation.

and q''_{evap} are the radiation and evaporation heat fluxes from the armour surface, respectively.

Both q''_{rad} and q''_{evap} are functions of the surface temperature and tend to be small at low temperatures. Thus, for simplicity, these fluxes can be calculated with small error based on the surface temperature at the previous time step in the finite difference calculations in order to avoid a cumbersome iterative procedure.

For a metal armour, when the melting point is reached, a melt layer is formed, as illustrated in Fig. 2. In this case, the melting point, T_m, is used to help in decoupling the solution of the heat conduction equation from that of the heat balance in the melt layer. At each time step, the heat conduction equation is first solved by setting the temperature equal to T_m at the melt layer/solid interface. Next, the conduction heat flux at the surface, q''_{cond}, is calculated based on the local temperature gradient in the solid:

$$q''_{cond} = -k\left(\frac{\partial T}{\partial x}\right)_{solid\text{-}surface}. \tag{3}$$

Finally, the incremental melt layer thickness, $\Delta\delta_m$, is calculated based on an energy balance at the surface using Eqs. (4)–(8):

$$q''_{pl} - q''_{rad} - q''_{evap} = \frac{k_m}{\delta_m}(T_s - T_m) + C_{p,m}\rho_m\frac{T_s - T_{s,old}}{2\Delta t}, \tag{4}$$

$$\frac{k_m}{\delta_m}(T_s - T_m) = \Delta\delta_m h_{fus}\rho + q''_{cond}, \tag{5}$$

$$q''_{pl} = f(T_s) \text{ (if vapour shielding effects are included)}, \tag{6}$$

$$q''_{rad} = \varepsilon\sigma\left(T_s^4 - T_{FW}^4\right), \tag{7}$$

$$q''_{evap} = 0.00432 \times 10^{B_i - A_i/T(K)}\sqrt{\frac{M_i}{T(K)}}\,h_v, \tag{8}$$

where k_m is the melt layer thermal conductivity; δ_m is the existing melt layer thickness; T_s is the melt layer surface temperature ($T_{s,old}$ refers to T_s at the previous time step); T_m is the melting point of the armour; $C_{p,m}$ is the specific heat of the melt layer; ρ_m is the density of the melt layer; Δt is the time increment; h_{fus} is the latent heat of fusion of the armour; ε is the surface emissivity; σ is the Stefan–Boltzmann constant; T_{FW} is the cooler first wall surface temperature to which q''_{rad} is radiated; q''_{evap} is calculated as the product of the maximum vacuum evaporation flux (kg/m^2 s) at T_s and the latent heat of vaporisation, h_v [13]; M_i is the molecular weight of the armour material; and A_i and B_i are parameters from the sublimation rate equation.

Note that in keeping with the objective of simplifying the model as much as possible while maintaining acceptable accuracy, the evaporation flux is estimated assuming no recondensation due to interaction with the vapour phase and the incoming plasma. This is deemed to be a reasonable approximation given the initial vacuum conditions; even, if the vapour pressure were such as to maximise the recondensation effect, the present estimate would be con-

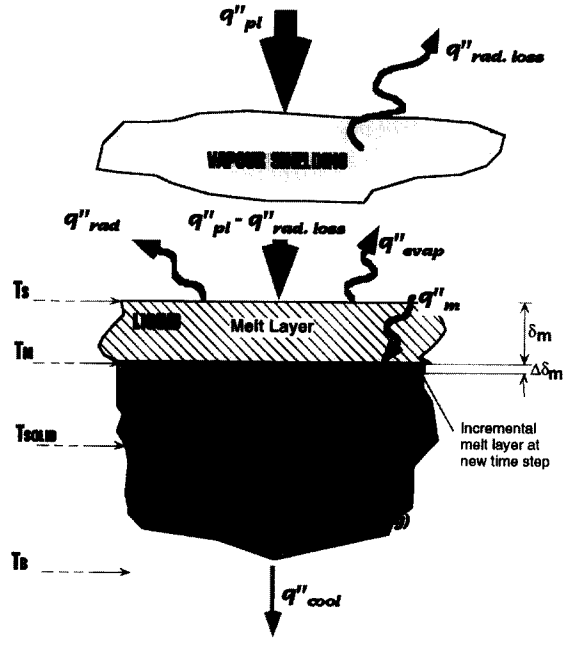

Fig. 2. Details of melt layer configuration for metal armour and heat fluxes illustrating vapour shielding effect and melt layer computation.

servative and overestimate evaporation by only $\simeq 20\%$ at the most [4].

To facilitate the computations, instead of solving the heat conduction equation in the melt layer which will require iterations, the conduction heat transfer through the melt layer is decoupled from the average inertial energy gain of the melt layer represented by the second right-hand side term in Eq. (4) since this term is relatively small compared to the other terms in the equation.

Since q''_{pl}, q''_{evap} and q''_{rad} are all functions of the melt surface temperature, T_s, Eq. (4) is solved iteratively in conjunction with Eqs. (6)–(8) to obtain T_s at the current time step. The value of T_s is then used in combination with the previously calculated q''_{cond} in estimating the incremental melt, $\Delta\delta_m$, from Eq. (5).

At each time step, the melt layer thickness is adjusted by the incremental melt as well as the incremental evaporated thickness loss inferred from Eq. (8). In addition, the model has the capability of accounting for total or partial melt layer loss by further adjusting the melt layer thickness at each time step to reflect the loss. The total thickness of the armour can also be adjusted accordingly to account for the corresponding effect of thickness reduction on the thermal response of the armour block.

2.2. Coolant side boundary condition

The boundary condition at the coolant side depends on the water coolant conditions. The coolant flowing through the PFC coolant channel will be subjected to the high heat fluxes and its conditions at the exit of the high heat flux region will be dependent on the coolant inlet conditions and the integrated heat load over the coolant channel.

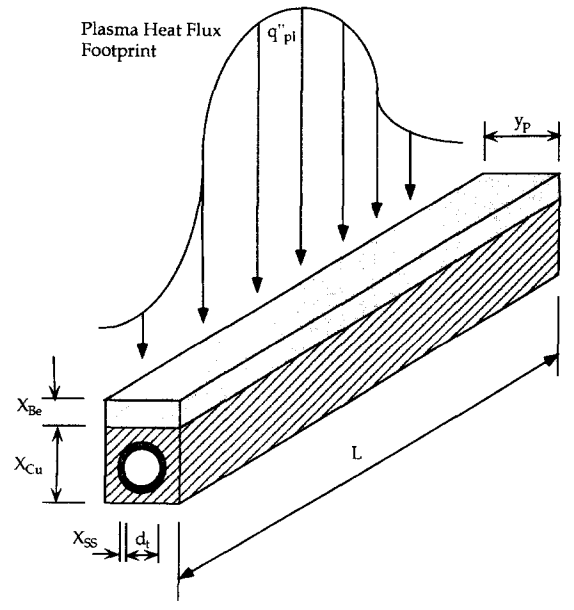

Fig. 3. Illustration of footprint of plasma incident heat flux on a typical plasma facing component configuration.

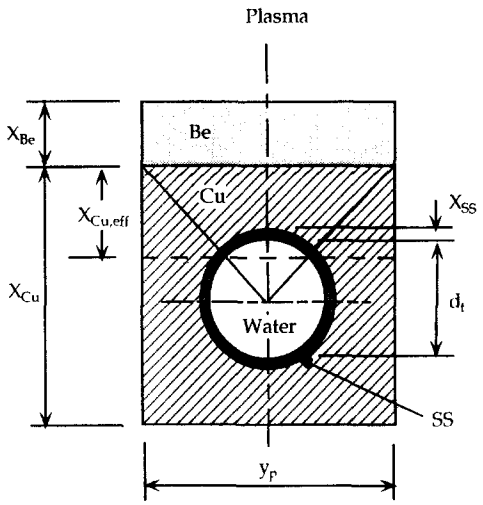

Fig. 4. Cross-section of an example PFC first wall configuration.

The plasma heat flux on a typical coolant channel would have a characteristic footprint peaking at a given location and decreasing away from the peak. An example footprint is illustrated in Fig. 3. The analysis focuses at the end, L, of the cooling channel where it is conservatively assumed that the peak heat flux occurs. The coolant bulk temperature there, T_b, can be calculated from the inlet channel conditions and the heat flow to the coolant:

$$T_b = T_{in} + \frac{f_p q_{cool} + q_{back}}{0.25\pi d_t^2 G C_p}, \tag{9}$$

where q_{cool} is the heat flow to the coolant based on the maximum plasma heat flux; f_p is a 'footprint' factor used to estimate the average coolant heat flux along the channel length accounting for the effect of plasma heat flux variation along the channel length); q_{back} is the heat flow from the volumetric heating in the structure at the back of the coolant channel; G is the average coolant mass velocity; C_p is the water specific heat; and d_t is the coolant channel diameter.

The above equation is for a circular coolant channel. The flow area would have to be adjusted accordingly for a rectangular channel.

Although the model is essentially based on a 1D geometry, a correction factor was included to account for 2D effects in the case of a circular channel. Such a case is illustrated in Fig. 4 for a typical PFC first wall configuration. It consists of a circular coolant channel, in this case made of stainless steel, embedded in a Cu matrix used as heat diffuser. A Be layer is placed on top of the Cu as armour material facing the plasma.

The geometry is modelled by assuming three material layers between the plasma and coolant, a Be layer of thickness x_{Be}, a Cu layer of effective thickness $x_{Cu,eff}$ (which can be defined separately to best model the 2D configuration) and a stainless steel layer of thickness x_{SS}. The neutron volumetric heat generation in these layers is included in the solution of Eq. (1). The total neutronic heat generation associated with the remaining part of the configuration is calculated as q_{back} and is used in estimating the total heat to the coolant in Eq. (9).

For both the heat flux through the stainless steel tube and to the coolant, two-dimensional peaking effects are accounted for by dividing the steel thermal conductivity and the convective heat transfer coefficient for the coolant by a factor f_{2D}. Typically, f_{2D} would be based on the ratio of the pitch to an assumed fraction of the coolant channel circumference, as will be discussed in Section 3.

Based on the coolant outlet temperature estimated from Eq. (9), the outlet coolant conditions can be determined. In its present form the code only considers single-phase and subcooled boiling conditions but not fully-developed boiling. For the subcooled boiling region, the circumferential non-uniformity of the heat flux to the coolant creates further difficulty in the analysis [14]. As a first order estimate, subcooled boiling empirical models developed for uniform heat fluxes are used in the code under the assumption that subcooled boiling behaviour in the higher heat flux regions would show similar characteristics to that under the same heat flux level but applied uniformly.

The Bergles and Rohsenow model [15] shown in Eq. (10) is used to determine the onset of nucleate boiling (ONB) and the Saha–Zuber model [16] shown in Eqs. (11) and (12) is used to determine the onset of fully-developed subcooled boiling (OFDSB) [17]:

$$(T_w - T_{sat})_{ONB} = 0.556\left(\frac{q''_{ONB}}{1082\,p^{1.156}}\right)^{0.463p^{0.0234}}$$

(valid for water over the pressure range of 0.1–13.8 MPa), (10)

where $(T_w - T_{sat})$, the difference between the wall temperature and the water saturation temperature at the outlet pressure, is in K, the coolant pressure, p, in bars and the heat flux, q'', in W/m^2. The ONB is determined by equating q''_{ONB} from Eq. (10) to the single-phase convective heat flux at the outlet (see Eq. (13)) and solving for the ONB wall temperature, $T_{w,ONB}$. If the wall temperature computed from the code at the outlet is lower than $T_{w,ONB}$, single-phase conditions exist. Otherwise, partially developed subcooled boiling conditions have been reached. As the heat flux to the coolant is increased, the transition from partially to fully developed subcooled boiling is then determined when the outlet bulk temperature exceeds the OFDSB outlet temperature based on the subcooling temperature difference in Eqs. (11) and (12):

$$(T_{sat} - T_b)_{OFDSB} = 0.0022\left(\frac{q''_{OFDSB} d_t}{k_b}\right) \quad \text{for Pe} < 70\,000, \tag{11}$$

$$(T_{sat} - T_b)_{OFDSB} = 153.8\left(\frac{q''_{OFDSB}}{GC_{p,b}}\right) \quad \text{for Pe} > 70\,000, \tag{12}$$

where b refers to the water bulk properties, $(T_{sat} - T_b)$ is the subcooling temperature difference at the outlet, G is the water mass velocity, and Pe is the Peclet number.

2.2.1. Single-phase conditions

The boundary condition at the coolant is quite simple in the case of single-phase flow. It is based on equating the conduction heat flux at the wall to the convective heat flux to the coolant, q''_{SP}:

$$-k_w\left(\frac{\partial T}{\partial x}\right)_w = q''_{SP} = \frac{h}{f_{2D}}(T_w - T_b), \tag{13}$$

where k_w is the thermal conductivity at the wall, h is the convective heat transfer coefficient, and T_w and T_b are the wall and water bulk temperatures, respectively. In the case of a stainless-steel tube, k_w would also be divided by the two-dimensional factor, f_{2D}. h is estimated from the Dittus–Boelter correlation:

$$\text{Nu} = \frac{hd_t}{k_f} = 0.023\text{Re}_f^{0.8}\text{Pr}_f^{0.33} \quad \text{for Re}_f > 6000,\ \text{Pr}_f > 0.7, \tag{14}$$

where all properties are evaluated at the mean film temperature in calculating the Reynolds number, Re_f, and the Prandtl number, Pr_f.

2.2.2. Subcooled boiling conditions

For fully developed subcooled boiling, the correlation of Thom et al. [18] is used to estimate the heat flux to the coolant, q''_{FDSB} (W/m^2), as a function of the wall temperature (K) and coolant pressure (bar):

$$(T_w - T_{sat})_{FDSB} = 22.65\left(q''_{FDSB} \times 10^{-6}\right)^{0.5} e^{-p/87}. \tag{15}$$

An effective heat transfer coefficient is introduced to help in applying the boundary condition to the solution of the finite difference equation:

$$-k_w\left(\frac{\partial T}{\partial x}\right)_w = q''_{FDSB} = h_{eff}(T_w - T_{sat}), \tag{16}$$

where h_{eff} is given by

$$h_{eff} = \frac{(T_w - T_{sat})e^{2p/87} \times 10^6}{22.65^2}. \tag{17}$$

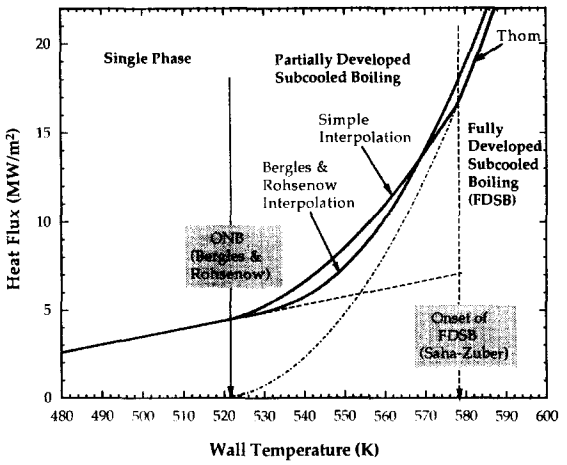

Fig. 5. Typical variation of heat flux with wall temperature for single-phase liquid and subcooled boiling regions ($T_b = 423$ K, $P = 3.6$ MPa, $T_{sat} = 517$ K, $G = 6420$ kg/m^2 s, single phase $h = 45{,}400$ W/m^2 K).

For simplicity, at each time step, h_{eff} could be calculated based on T_w at the previous time step or, if better accuracy is required, by iteration.

For the partially developed subcooled boiling region, typical effective heat transfer coefficients used are almost purely empirical fits between the single-phase liquid (SP) and fully-developed subcooled boiling regimes [14]. A popular one is the Bergles and Rohsenow fit [15,17], as illustrated in Fig. 5 which shows a typical plot of heat flux as a function of wall temperature for the single-phase liquid and the partially and fully-developed subcooled boiling regimes for example coolant conditions. However, the Bergles and Rohsenow interpolation formula results in a highly non-linear boundary condition at the coolant. It was decided to develop a linear interpolation formula with minimal departure from the Bergles and Rohsenow one to help simplify the finite difference solution procedure.

The proposed interpolation formula in the partially-developed subcooled (PDSB) region is as follows:

$$q''_{PDSB} = q''_{SP} + (q''_{FDSB} - q''_{SP})_{OFDSB} \times \frac{q''_{FDSB} - q''_{FDSB,ONB}}{q''_{FDSB,OFDSB} - q''_{FDSB,ONB}}. \quad (18)$$

On simplification, the boundary condition in the PDSB region can be written as

$$-k_w\left(\frac{\partial T}{\partial x}\right)_w = q''_{PDSB} = \frac{h}{f_{2D}}(T_w - T_b) + h_{eff}(T_w - T_{w,ONB}), \quad (19)$$

where h_{eff} in this case is given by

$$h_{eff} = \frac{(q''_{FDSB} - q''_{SP})_{OFDSB}}{q''_{FDSB,OFDSB} - q''_{FDSB,ONB}}(T_w + T_{w,ONB} - 2T_{sat}) \times \frac{e^{2p/87} \times 10^6}{22.65^2}. \quad (20)$$

At each time step, the solution of the finite difference equation (Eq. (1)) based on the PDSB boundary condition proceeds as follows. First q''_{FDSB} at OFDSB is determined by equating the heat flux from Thom's equation (Eq. (15)) to the heat flux from Saha–Zuber (Eqs. (11) and (12)). An energy balance similar to that of Eq. (9) is used to calculate the water bulk outlet temperature, T_{out}, as a function of the heat flux to the coolant:

$$q''_{FDSB,OFDSB} = \frac{T_{sat} - T_{in} - C_{q,c}}{C_{S-Z} + C_q}, \quad (21)$$

where

$$C_{S-Z} = \frac{0.0022 d_t}{k_f} \quad \text{for Pe} < 70\,000,$$

$$C_{S-Z} = \frac{153.8}{GC_{p,f}} \quad \text{for Pe} > 70\,000, \quad (22)$$

$$C_{q,c} = \frac{q_{back}}{0.25\rho v \pi d_t^2 C_p}, \quad (23)$$

$$C_q = \frac{2f_p L}{\rho v d_t C_p}. \quad (24)$$

Then, based on this $q''_{FDSB,OFDSB}$ value, T_w at OFDSB is calculated from Thom's equation (Eq. (15)). From this value of T_w and from T_{out} at OFDSB, $q''_{SP,OFDSB}$ can be calculated from Eq. (13). Similarly, by equating q''_{SP} from Eq. (13) to q''_{ONB} from Bergles and Rohsenow Eq. (10), T_w at ONB can be calculated. Using this value of T_w in Thom's equation, $q''_{FDSB,ONB}$ can also be calculated.

Again, as for the FDSB case, T_w figures in the h_{eff} expression but as a relative term whose effect tends to be mitigated by the presence of the other variables, $T_{w,ONB}$ and T_{sat}. For simplicity, the value of T_w at the previous time step can be used to advance the implicit finite difference solution, provided any loss in accuracy is acceptable. Otherwise, a lengthier iterative procedure would be required.

For the typical example case plotted in Fig. 5, the simple interpolation formula is also plotted and can be seen to be in reasonable agreement with the Bergles and Rohsenow one. In addition, in contrast to the latter, the simple interpolation formula approaches exactly Thom's formula for fully-developed subcooled boiling at the onset of FDSB, which also help for a smoother solution.

3. Model calibration and validation

The heat conduction part of the code was first verified by a successful comparison with analytical results for a simple transient condition case. The adequacy of the 2D geometry factor used to estimate the heat flux through the channel wall and to the coolant from the 1D calculations was then assessed by comparison with 2D ANSYS [9] finite element results for a typical steady state situation. The analysis was based on the first wall geometry shown in Fig. 4 and the results are summarised in Fig. 6 for the typical PFC parameters summarised in the figure caption. Results are shown for cases with SS and Cu channels, respectively. For both cases, the ANSYS results fall between the RACLETTE results based on half-channel-circumference 2D scaling (f_{2D} = pitch to half channel circumference ratio) and results based on full-circumference scaling (f_{2D} = pitch to full channel circumference ratio). For the case with SS channel which provides a higher thermal resistance and thus a better diffusion of the heat flux around the channel, the RACLETTE results based on full circumference scaling tend to be slightly closer to the ANSYS results while for the Cu channel case, the RACLETTE results based on half-circumference scaling tends to be closer to the ANSYS results. It seems that a 2D scaling half way in between would provide a more accurate estimate. However, for the typical parameters considered, the Be temperature overprediction based on half circumference scaling is within $\simeq 5\%$ for the Cu channel case and within $\simeq 10\%$ for the SS channel case and, to be conservative, it was decided to adopt it as the default scaling subject to adjustment based on the particular geometry to be analyzed.

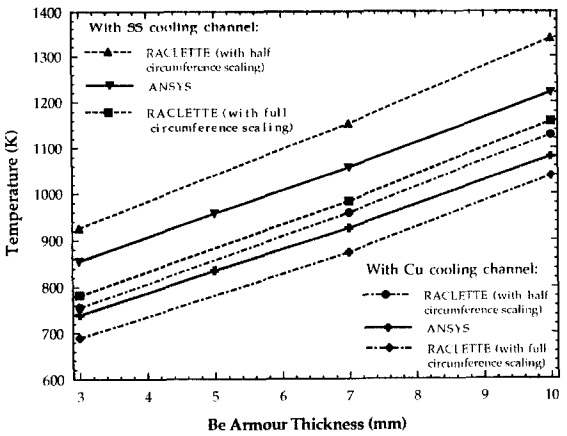

Fig. 6. Maximum steady-state Be armour temperature as a function of Be armour thickness based 2D ANSYS finite element analysis and RACLETTE using different 2D scaling for cases with SS and Cu channels ($q''_{pl} = 5$ MW/m^2, $X_{Cu} = 17$ mm, $X_{SS} = 0.5$ mm, $d_t = 10$ mm, $y_p = 20$ mm, Cu minimum thickness = 3 mm, $T_b = 150$°C).

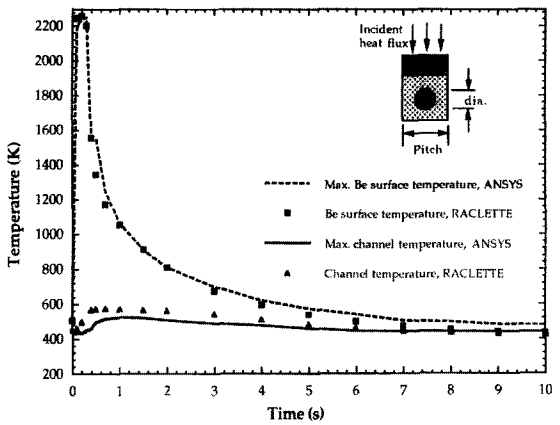

Fig. 7. Comparison of ANSYS and RACLETTE results for the histories of maximum Be armour temperature and coolant channel temperature following a plasma energy transient of 60 MJ/m^2 over 0.3 s assuming no shielding effect. (Nominal $q''_{pl} = 0.5$ MW/m^2, $X_{Be} = 5$ mm, $X_{Cu} = 17$ mm, $X_{SS} = 1$ mm, $d_t = 10$ mm, $y_p = 20$ mm, Cu minimum thickness = 3 mm, $T_b = 140$°C.)

Next, RACLETTE was calibrated for a transient case again by comparison with a 2D ANSYS analysis which was adapted to include the melting process through a correction of the Be enthalpy [10]. The results for the Be surface temperature and coolant channel temperature histories are shown in Fig. 7 based on the assumed parameters listed in the figure caption. From the figure, it can be seen that the Be surface temperature predicted by RACLETTE is very close to the 2D case indicating that the heat flux through the Be region to the Cu heat sink is virtually uni-dimensional. RACLETTE tends to overpredict the coolant channel temperature in the early stages of the transient. This is partly due to the half circumference 2D factor used which tends to be conservative. Overall, the results are in reasonable agreement which is in line with the objective of favourising model simplification, convenience and computing speed for an acceptably small accuracy loss. As a comparison here, running the 2D model for this case would require 10 to 50 times the computing time needed for RACLETTE.

Finally, RACLETTE was used to analyse and interpret some results available from high power tests performed in the JET neutral beam Be test facility on 10 mm thick beryllium tile brazed to an actively cooled hypervapotron copper heat sink and subjected to high power beam pulses derived from a JET positive ion neutral injector (PINI). Detailed results and discussions can be found in Refs. [19,20]. The test was performed to establish if the tiles could be heated up to surface melting without being damaged. This type of heat loads are anticipated to simulate the ITER fault condition, when the radiative divertor is lost and the plasma burns through the armour plate. The expectation is that a radiative cloud forms due to the evaporation from the beryllium armour which reduces the

impinging power density and thus limit the damage to the armour tile. The vapour shielding itself could not be tested in this experiment due to the high particle energy.

The average power density on the test section was varied by modulating the beam (on/off modulation) with a peak power of about 20.5 MW/m^2. The modulation sequence used was: (1) Modulation with 18 ms on every 80 ms for 4 s (average power density is 22.5% of the peak power density, i.e $\simeq$4.2 MW/m^2) followed by (2) beam full on for up to 1.3–1.5 s followed by (3) modulation with 12 ms on every 34 ms (average power density is 35% of the peak power density, i.e., 7–8 MW/m^2) for approximately 2 s. In comparing the results, one should keep in mind that the power setting and the measured temperature (inferred by correcting values obtained with an IR camera) are not too accurate, particularly the latter, because of the irreversible change in emissivity of the Be when it reaches temperatures above 1000°C (which was not considered in the calculations). The measured and calculated surface temperatures are shown in Fig. 8. Because of the uncertainties of the nominal power density when the beam is fully on and during the preheat-phase which are not well known from the experiment, two different cases were analysed and the sensitivity of the melting and re-solidification in the model to the power setting is clearly seen in the plot. Beginning of melting and resolidification are reasonably well reproduced for the case of 20.5 MW/m^2 and 5.5 MW/m^2, respectively, for the second and third phases described above. For this case, the surface remains above melting for about 700 ms and the calculated melt depth is 0.49 mm which is in good agreement with the experimentally inferred value of 0.42–0.53 mm.

4. Parametric analyses

In this section, the capabilities of the model are illustrated through a number of parametric studies from which trends in responses of PFCs with various armour thicknesses to different energy deposition transients are discussed. The analyses focus on Be armour which is a major candidate for use in ITER PFC and which, as a metal armour, represents also a more challenging case since armour melting must be accounted for in the analysis.

High energy deposition on PFCs could lead to severe consequences to the Be armour itself through melting and vaporisation but, potentially, to the PFC block also due to high coolant heat flux levels, high interface temperatures, thermal stress and resulting crack propagation. To help prevent unacceptably high Be/Cu heat sink joint interface temperatures and coolant heat fluxes, the Be armour could be designed to be sufficiently thick to provide inertial cooling that would, over time, diffuse the heat flux seen by the interface and coolant, albeit with the penalty of higher melting and vaporisation.

In this section, example histories of heat fluxes, temperatures, vaporisation depth and melt layer thickness are first shown for a sample case. A description of parametric analyses then follows, focusing on the determination of the effect of the Be thickness and of the magnitude and

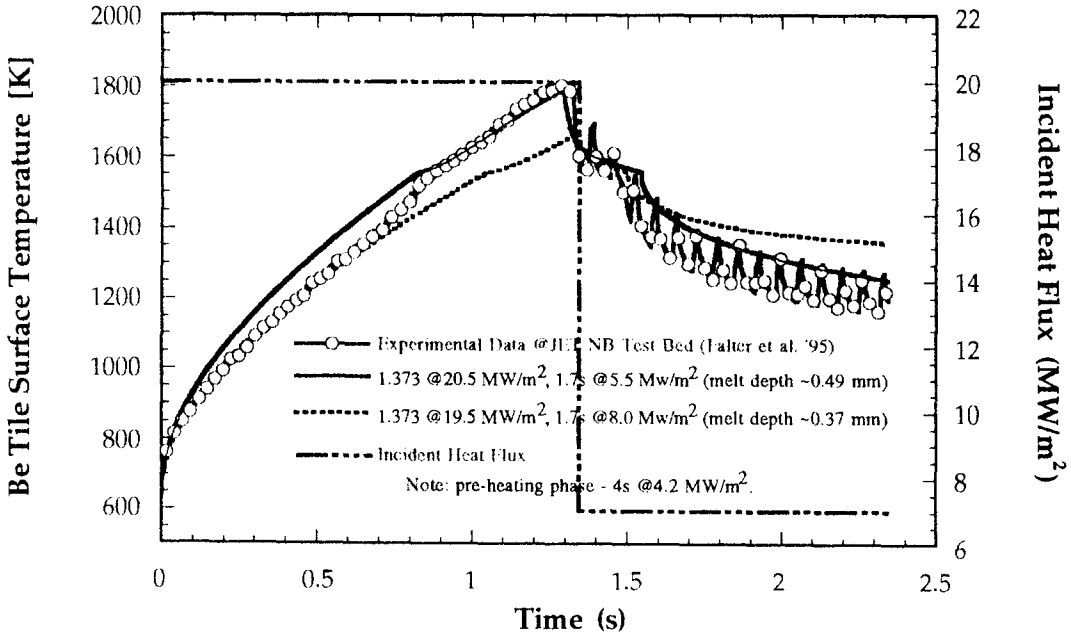

Fig. 8. Measured and calculated Be surface temperature history for a 10 mm Be block subject to high heat flux transients in the JET neutral beam Be test bed [19,20].

Table 2
Reference parameters for example case considered for the analysis

Coolant inlet temperature	413 K
Coolant pressure	3.6 MPa
Coolant mass velocity	2000 kg/m^2 s
Be thickness	5 mm
Cu block thickness	20 mm
SS thickness	1 mm
Channel length	1.5 m
Footprint fraction	1
Be volumetric heat generation	10 MW/m^3
Cu and SS volumetric heat generation	15 MW/m^3
Nominal plasma heat flux	0.5 MW/m^2
Conditions resulting from VDEs	
Plasma energy density	60 MJ/m^2
Energy deposition time	0.3 s
Vapour shielding effects	no
Beryllium properties	
Thermal conductivity, $f(T)$	183 W/m K at room temperature 60 W/m K at T_m
Heat capacity, $f(T)$	1760 kJ/kg K at room temperature 3400 kJ/kg K at T_m
Density	1850 kg/m^3
Melting point	1556 K
Latent heat of fusion	1.3 MJ/kg
Latent heat of vaporisation	36.6 MJ/kg
Emissivity, ε	0.61
Molecular weight	9
Parameters in sublimation flux equation (as part of Eq. (8))	
A_i	16 720 K
B_i	11.61

deposition time of the transient plasma energy on the extent of Be melting and vaporisation and on the resulting interface temperatures and coolant heat flux. Finally, the possible mitigating effects of vapour shielding are addressed and discussed. Unless otherwise specified, the analyses are based on the PFC parameters listed in Table 2, which would be typical of a primary first wall or limiter case under a VDE transient, for instance. Note that the plasma heat flux and volumetric heat generations are all set to zero following the transient under the assumption of plasma shutdown following such an event.

At this stage, a thermal stress computation capability has not been included in the code. It is also not clear what are the acceptable levels of thermal stress at the Cu heat sink/coolant channel interface and, in particular, at the Be/Cu heat sink interface. These need to be better characterised experimentally. For the analyses presented here to illustrate parametric trends, the heat flux to the coolant is used as a general measure of the heat flux and thermal gradients through the PFC block. Note that very high coolant heat fluxes would result in full saturation boiling for the coolant, which is not within the scope of the model. Thus, results shown here corresponding to high coolant heat fluxes are meant to be illustrative of the parametric trends only and not accurate in the absolute term.

4.1. Histories of heat fluxes, temperatures, and melt and evaporated thicknesses for sample case

Fig. 9 shows histories of heat fluxes following an energy transient based on the example parameters listed in Table 2. The initial inward conduction flux from the Be surface is high, $\simeq 200$ MW/m^2 and the temperature gradient at the surface is at its maximum with the surface temperature at the melting point and the rest of the Be still at its low initial temperature. As the Be bulk temperature increases, the conduction flux decreases. Initially, the effective melt heat flux is high but decreases as the evaporation heat flux increases. After about 0.03 s, the evaporation heat flux is the major heat flux component. The black-body radiation heat flux is comparatively small and is not significant in this case. Note that, at the end of the energy deposition transient (0.3 s), the effective melt heat flux becomes artificially negative illustrating heat generation to the block as the melt layer resolidifies.

Fig. 10 shows the history of the temperatures of the melt front, Be melt/solid interface, Be/Cu heat sink interface, heat sink/coolant channel interface, channel inner wall, and coolant bulk for the same case. The surface temperature reaches the melting point (1556 K) very quickly at which time the melt/solid interface temperature is clamped. The melt front temperature continues to increase until the corresponding evaporation heat flux, in combination with conduction through the melt layer, is high enough to account for the plasma heat flux. The temperatures at the other locations inside the PFC block show a typical thermal diffusion thermal behaviour. They all peak sometime after the energy deposition has stopped

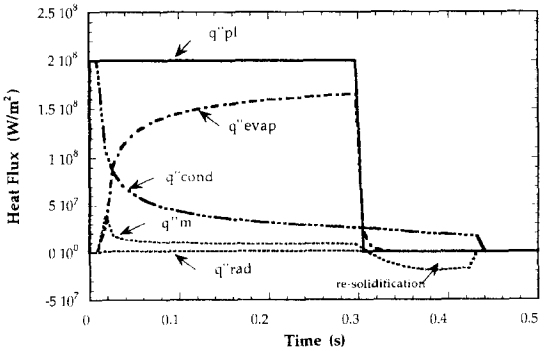

Fig. 9. Histories of plasma, evaporation, radiation, solid surface conduction and effective melt heat fluxes following a plasma energy deposition transient of 60 MJ/m^2 over 0.3 s for the example case parameters listed in Table 2.

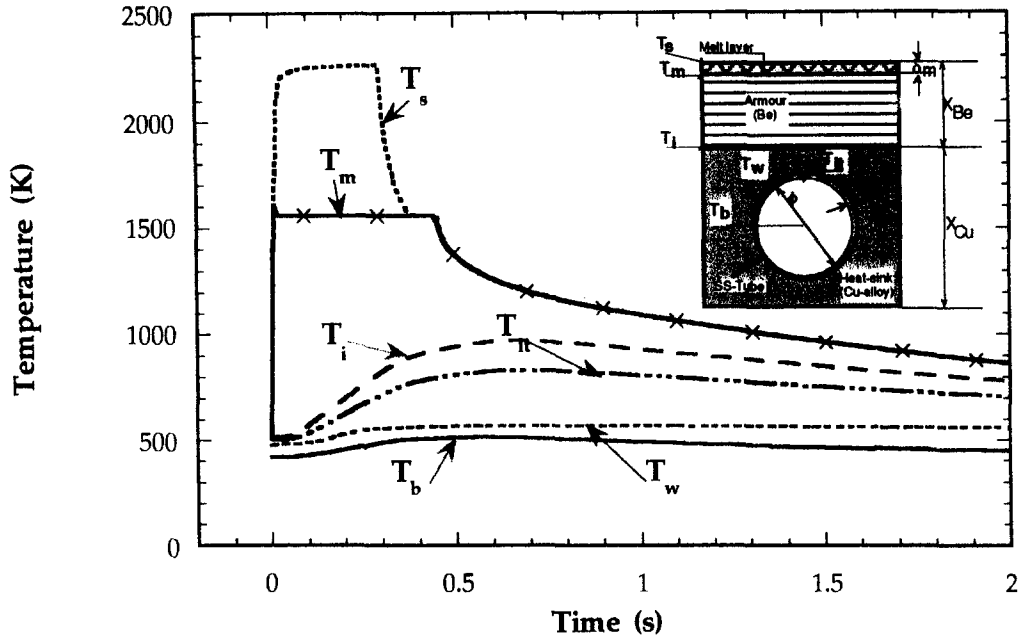

Fig. 10. Histories of temperatures at melt front (T_s), Be melt/solid interface (T_m), Be/Cu heat sink interface (T_i), heat sink/coolant channel interface (T_{it}), channel inner wall (T_w) and coolant bulk (T_b) following a plasma energy deposition transient of 60 MJ/m^2 over 0.3 s for the example case parameters listed in Table 2.

due to the inertial cooling effect whereby the heat flux diffuses through the PFC block to the coolant over a longer time and at a lower level due to the PFC block thermal resistance and heat capacity. In this case for the relatively thin armour and corresponding thermal resistance, all temperatures peak within 1 s. For thicker armour and/or longer deposition time the temperature peaking would occur after a longer time.

Fig. 11 shows the corresponding histories of melt layer thickness and effective evaporated thickness. The melt layer thickness increases rapidly at first and then at a lower rate as evaporation plays an increasingly more important role as seen by the increasing effective evaporated layer thickness. In this case, the maximum melt layer and effective evaporation thicknesses are about 0.8 and 0.65 mm, respectively. The melt layer is assumed to re-solidify in this case and the melt layer thickness decreases to zero very rapidly following the transient. It is not clear whether the assumption of no melt layer loss is reasonable. If the molten Be flows or is splashed out by the on-going energetic process, a significant loss of armour can occur. As will be discussed later, the evaporated and melt layer thickness loss can be significantly mitigated if vapour shielding occurs. Experimental data are required to verify the behaviour of the melt layer as the level of melt layer loss will substantially determine the need and frequency of surface repair required.

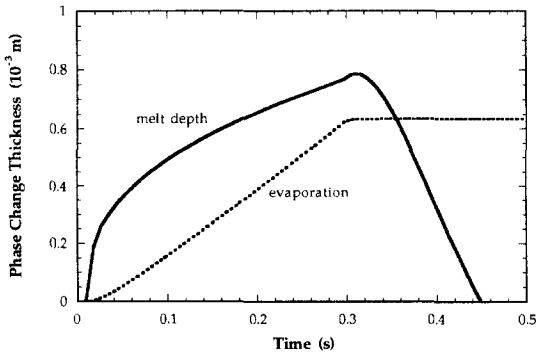

Fig. 11. Histories of Be melt layer and effective evaporated layer thicknesses following a plasma energy deposition transient of 60 MJ/m^2 over 0.3 s for the example case parameters listed in Table 2.

4.2. Effect of variation in Be thickness

The consequences of concern from transient plasma energy deposition include high material temperatures and temperature gradients, in particular at the Cu/Be interfaces where the material bonding could be affected, and high heat flux to the coolant. Both the maximum coolant heat flux and Be/Cu temperature and temperature gradient occur some time after the energy deposition transient depending on the thermal diffusion time constant of the PFC block.

High coolant heat flux could result in local boiling which, by itself, is acceptable as long as it can be resorbed.

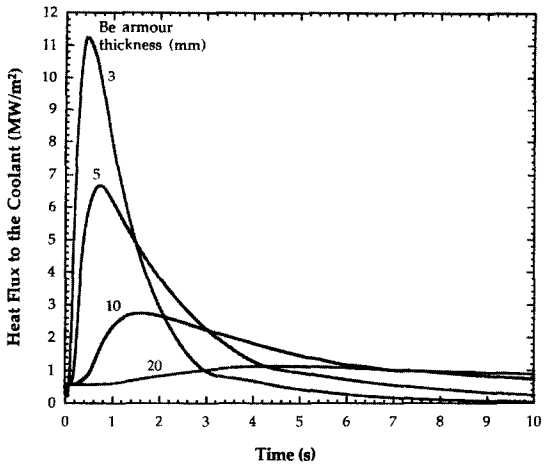

Fig. 12. Histories of heat flux to the coolant following a plasma energy deposition transient of 60 MJ/m^2 over 0.3 s for different Be armour thicknesses and for the example case parameters listed in Table 2.

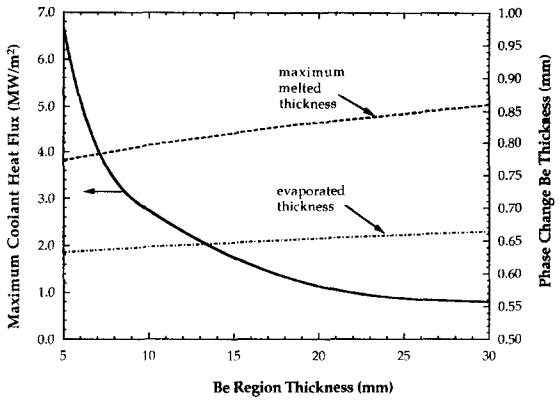

Fig. 13. Maximum coolant flux (normalised to coolant channel pitch) and Be melt and effective evaporated thicknesses as a function of Be region thickness for the example case parameters listed in Table 2.

Of concern is the increase in flow resistance associated with two-phase flow which can result in starving of the channel in the case of parallel flow. If there is enough inertial energy in the first wall region, dryout, or at least very high material temperatures, could result. A full integration of the different thermal-hydraulic phenomena resulting from the transient plasma energy deposition, including pressure drop and heat transfer variation, to the overall analysis can be quite complex and is addressed in Ref. [12].

Fig. 12 shows the coolant heat flux histories for different Be armour thicknesses based on the parameters listed in Table 2. The figure illustrates the inertial effect of the armour thickness. An increase in Be thickness results in an increase in the PFC block thermal resistance which diffuses the energy to the coolant over a longer time and reduces the peak coolant heat flux. Note that the time scale for the coolant heat flux would also increase with increasing plasma energy deposition time.

Fig. 13 summarises the effect of Be thickness on the maximum coolant heat flux and on the melted and evaporated thicknesses for the parameters listed in Table 2 (under the assumption of no melt layer loss). The maximum heat flux through the armour to the coolant decreases substantially with increasing Be thicknesses due to the inertial cooling effect. Conversely, as the heat conduction resistance increases with the Be layer thickness, a lower fraction of the incident heat flux is transported by conduction. This results in an increase in evaporation and melting as shown in the figure.

4.3. Effect of plasma energy deposition time

Fig. 14 shows the maximum heat flux to the coolant as a function of the energy deposition time for a deposited plasma energy density of 60 MJ/m^2 and the parameters listed in Table 2. Also shown are the maximum Be melt layer and effective evaporated thicknesses. Again, these results should be viewed as illustrative particularly for short energy deposition times since vapour shielding is not included.

The figure illustrates the trend that at short energy deposition time (much smaller than the conduction time constant), the effective heat flux is so high that it results in high evaporation. Most of the energy is removed in this way and the resulting maximum heat flux through to the coolant is small. As the energy deposition time is increased, the heat flux level decreases and the heat conducted through the melt layer and solid Be becomes comparatively larger. The maximum melt layer thickness and heat flux to the coolant increase up to a peak at a deposition time of $\simeq 2$ s. Conversely, since the plasma heat flux can increasingly be conducted through the melt

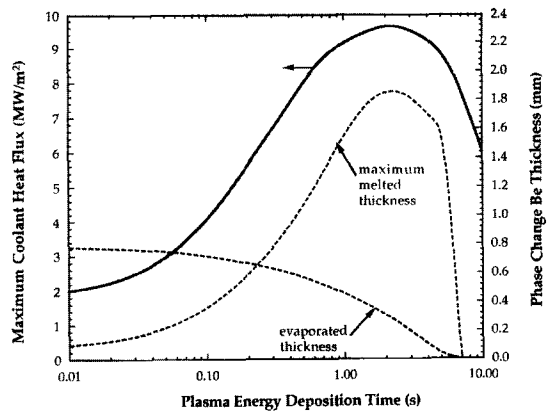

Fig. 14. Maximum heat flux to the coolant and Be melt and effective evaporated thicknesses as a function of energy deposition time.

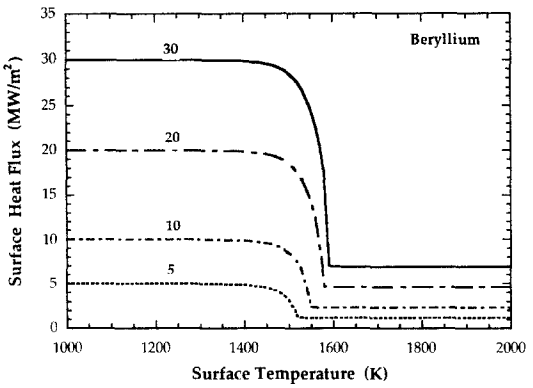

Fig. 15. Surface heat flux as a function of Be surface temperature based on vapour shielding effect [21].

layer and solid Be, evaporation decreases with increasing deposition time. At higher deposition times, the effective plasma heat flux can be entirely conducted through the PFC block without Be evaporation and/or melting and the evaporated and melt layer thicknesses drops to zero within $\simeq 7$ s. The coolant heat flux also decreases as the plasma heat flux decreases with increasing deposition time for a given deposited plasma energy density. The maximum temperature of the Cu/Be interface, not shown in the figure, follows the same trend as the maximum coolant heat flux, peaking to a value of $\simeq 1173$ K at an energy deposition time of $\simeq 2$ s.

4.4. Effect of deposited plasma energy density and of vapour shielding

The incident heat flux could be attenuated to some extent by low density vapour shielding effects. These may arise as the armour surface temperature increases due to vaporisation of material from the surface, leading to a conversion of some of the incident power to plasma radiation, a fraction of which continues to fall on the plate. Recently, estimates of this vapour shielding effect were made for a number of plasma heat flux cases based on simple plasma physics considerations [21]. The reduction of the incident plasma heat flux from radiation losses near a Be target is shown in Fig. 15 as a function of the target surface temperature for different plasma heat flux levels. Up to a temperature of about 1500 K, the evaporation rate is small and, as shown in the figure, the surface heat flux remains at its peak level. Then, as the evaporation flux increases substantially over a surface temperature range of 1500 to 1580 K (around the melting point of Be), the heat flux falls rapidly to about 25% of its peak value. These results were used to determine the effect of vapour shielding on the Be PFC block behaviour. The results are illustrated in Fig. 16 which shows the maximum heat flux to the coolant and the melt and evaporated thicknesses as a function of the deposited plasma energy density for a deposition time of 0.3 s, for cases with and without vapour shielding.

From Fig. 16, the coolant heat flux can be seen to increase rapidly with the deposited energy density at first, but increasingly slowly at higher energy flux levels. At lower energy densities, there is little or no melting and evaporation. As the energy density increases above about 15 MJ/m^2 in this case, melting increases rapidly and levels off at about 0.78 mm at an energy density of 20 MJ/m^2. At higher energy densities, the additional energy is virtually accommodated solely by vaporisation and the evaporated thickness increases roughly linearly with the energy density.

From the figure, it is interesting to see that inclusion of the vapour shielding effect results in much lower Be evaporated thicknesses and, at lower energy densities, melting thicknesses also. However, the decrease in maximum heat flux to the coolant, as a measure of the PFC block temperature level and gradient, is not as marked particularly at the lower energy densities. This can be explained by the observation that at an effectively higher plasma heat flux, only part of the heat flux can be conducted through the surface; the rest contributes to evaporation and melting. As the plasma heat flux is reduced due to vapour shielding, the conduction component is still about the same whereas the evaporation and melting components are significantly reduced.

4.5. Design implications of integrated consideration of energy transient and Be armour

As an example of the design implications of the VDE effect on the PFC armour, one could consider the combination of plasma heat flux and deposition time required to avoid serious consequences to the PFC block for a given

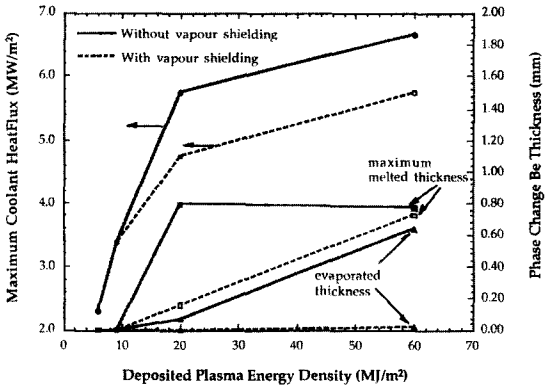

Fig. 16. Maximum heat flux to the coolant and Be melt and effective evaporated thicknesses as a function of plasma energy density for an energy deposition time of 0.3 s and the assumed parameters from Table 2.

Be armour thickness. As mentioned earlier, the coolant heat flux level can be regarded as a measure of the temperature level and gradient through the PFC block and as an indication of the coolant conditions and heat transfer characteristics. The heat flow to the coolant will determine the coolant temperature, and, particularly in the case of two-phase flow, its pressure and mass velocity also. These evolving coolant conditions would determine the coolant critical heat flux (CHF) conditions following the energy deposition transient. If the coolant heat flux exceeds the CHF conditions, the heat removal capability of the coolant can be severely degraded leading to potentially unacceptable level of temperature throughout the CFC block and in particular at the armour/heat sink interface. Modeling of these phenomena is quite complex and is described in detail in Ref. [12] for specific ITER PFC applications.

For given coolant inlet conditions, the coolant temperature and regime would depend not only on the coolant heat flux but on the time over which it stays at a high level and on the footprint of the energy deposition. Here, as an illustration, it is assumed that the coolant heat flux must stay below $\simeq 3.4$ MW/m^2 (roughly corresponding to saturation for a 1 m long channel) to avoid any serious consequences. Fig. 17 shows the combinations of plasma heat flux and deposition time required for the coolant heat flux to reach this maximum value for Be armour thicknesses of 5 and 10 mm. Also shown in the figure are the combinations of plasma heat flux and deposition time corresponding to deposited plasma energy densities of 20 and 60 MJ/m^2, respectively.

At short energy deposition times, the coolant heat flux becomes increasingly independent of the plasma heat flux, and increasing the plasma heat flux results only in increasing melting and evaporation. Within the time scale shown in the figure, this is better illustrated by the 10 mm Be case. Conversely, at long energy deposition times, the given coolant heat flux becomes independent of the deposition time since the plasma heat flux is entirely conducted to the coolant. For a given energy density, one can select a minimum armour thickness to avoid the severe consequences resulting from too large a heat flux through the PFC block to the coolant, independently of the energy deposition time. Assuredly, this must assume that the loss of armour through evaporation and melting can be accommodated by additional sacrificial armour thickness and/or through surface repair such as plasma spray. For instance, for the example shown in the figure, the assumed maximum coolant heat flux limit could be satisfied with a minimum armour thickness of $\simeq 10$ mm for an energy density of 20 MJ/m^2 regardless of the energy deposition time. For an energy density of 60 MJ/m^2, the Be thickness would have to be higher to satisfy this maximum heat flux criterion.

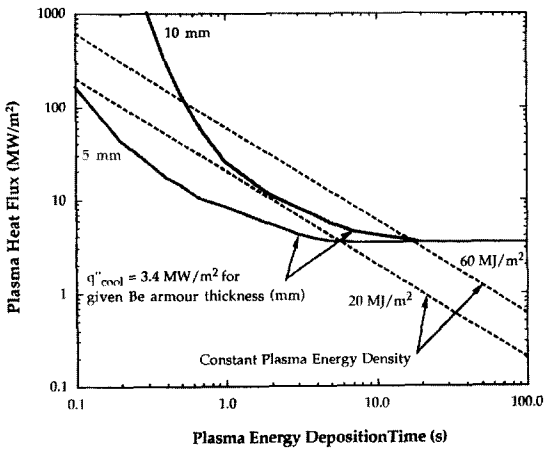

Fig. 17. Combinations of plasma heat flux and deposition time required for the coolant heat flux to reach an assumed maximum value of 3.4 MW/m^2 for Be armour thicknesses of 5 and 10 mm. Also shown are the combinations of plasma heat flux and deposition time corresponding to plasma energy densities of 20 and 60 MJ/m^2.

5. Summary

'Slow' high power plasma energy deposition on PFCs, as could occur, for example, in the case of a plasma VDE, can lead to surface evaporation and melting, high coolant heat flux levels, high armour/heat sink interface temperatures, thermal stress and resulting crack propagation. RACLETTE, a simple but comprehensive model that could be used quickly and conveniently, was developed to help understand the behaviour and perform design analysis of PFCs under such transient energy deposition. It includes all the key surface processes such as evaporation, melting, and radiation, and their interaction with the PFC block thermal response and the coolant behaviour. The model was first calibrated and validated by comparison with analytical results, with multi-dimensional finite element results and with experimental results.

Parametric studies were then carried out to evaluate the effect of the plasma energy density and deposition time and of the Be layer thickness on the conducted heat fluxes in the solid and on the level of Be melting and evaporation. The incident heat flux could be attenuated to some extent by low density vapour shielding effects. Consequences of such effects on the PFC block transient response were also investigated based on input from a separate model.

The following observations can be made from the results of the analyses.

- For a given energy density, at short deposition times, most of the energy goes to evaporate Be and the heat flux through the PFC block is small. As the deposition time

increases up to about 2–3 s for an energy density of 60 MJ/m^2, the maximum conducted heat flux increases to a peak and then falls down at higher deposition times. The melt layer thickness also peaks at about the same time and then rapidly falls to zero as the effective plasma heat flux can be entirely accommodated by the conduction flux through the armour. The evaporation flux falls continuously with increasing deposition time as an increasing fraction of the deposited power is accommodated by melting and conduction.

- For a given plasma energy density and deposition time, as the Be thickness is increased, the inertial cooling effect increases and the resulting maximum conducted heat flux decreases as the energy diffuses over a longer time to the coolant. If one assumed a maximum allowable coolant heat flux of $\simeq 3.4$ MW/m^2 to prevent saturation conditions, a minimum Be thickness of $\simeq 10$ mm would be required for an energy density of 20 MJ/m^2 irrespective of the energy deposition time. This assumes no constraint on the extent of evaporation and melting. This result is intended as an illustration of the design implication of VDE-type transient energy deposition on PFC armour thickness. A more detailed analysis of such a case for specific ITER PFCs is presented in part II of this paper [12].
- For given energy deposition time and Be thickness, the coolant heat flux increases rapidly with the plasma energy density at first but increasingly slowly at higher energy densities. At lower energy densities, there is little or no melting and evaporation. For the example case considered, as the energy density increases above about 15 MJ/m^2, melting increases rapidly and levels off at about 0.78 mm at an energy density of 20 MJ/m^2. At higher energy densities, the additional energy is virtually accommodated solely by vaporisation and the evaporated thickness increases roughly linearly with energy density.
- Vapour shielding effects substantially reduced armour melting and evaporation but tend to have a smaller effect on the heat flux conducted through the solid.
- Experimental data for PFC armour under high heat flux including characterization of the extent of melting and evaporation are needed. These would help in better evaluating the accuracy and adequacy of models such as RACLETTE and in understanding the interrelated phenomena involved.

Further developments are planned for the model. A more detailed treatment of the coolant behaviour, including time-dependent heat transfer, pressure drop and CHF evaluations, is presented in part II of this paper [12]. Based on these improved model capabilities, detailed analyses of the response of specific ITER PFCs are carried out and recommendations proposed to help in the selection of armour material and thickness.

Other improvements contemplated include estimating the thermal stress and strain at key locations, such as at the Be/Cu interface, which would shed more light on the consequences of high heat flux through the PFC block.

6. Nomenclature

C_p	specific heat of the material;
$C_{p,m}$	specific heat of the melt layer;
C_q	parameter defined in Eq. (24) and used to calculate $q''_{FDSB,OFDSB}$
$C_{q,c}$	parameter defined in Eq. (23) and used to calculate $q''_{FDSB,OFDSB}$
C_{S-Z}	parameter defined in Eq. (22) and used to calculate $q''_{FDSB,OFDSB}$
d_t	coolant channel diameter;
f_p	plasma footprint factor;
f_{2D}	geometry factor to account for 2D effects;
G	coolant mass velocity;
h	convective heat transfer coefficient;
h_v	latent heat of vaporisation of the armour material;
h_{fus}	latent heat of fusion of the armour material;
k	material thermal conductivity;
k_m	melt layer thermal conductivity;
L	channel length;
M_i	molecular weight of the armour material;
Nu	Nusselt number;
p	pressure;
Pe	Peclet number;
Pr	Prandtl number;
q_{cool}	heat flow to the coolant based on maximum plasma heat flux;
q_{back}	heat flow to the coolant from volumetric heating in back structure;
q'''	heat generation per unit volume;
q''	heat flux;
q''_{cond}	conduction heat flux from armour solid surface;
q''_{evap}	effective evaporation heat flux;
q''_{FDSB}	coolant heat flux in fully developed subcooled boiling;
q''_{OFDSB}	coolant heat flux at onset of fully developed subcooled boiling;
q''_{ONB}	coolant heat flux at onset of nucleate boiling;
q''_{pl}	plasma heat flux;
q''_{rad}	radiation heat flux;
Re	Reynolds number;
T	temperature;
T_b	coolant bulk temperature;
T_{FW}	first wall surface temperature to which q''_{rad} is radiated;
T_{in}	coolant inlet temperature;
T_m	melting point of the armour material;
T_{out}	coolant outlet temperature;
T_s	melt layer surface temperature;

t time;
y_p coolant channel pitch;
x distance perpendicular to armour surface;
X_{Cu} thickness of Cu heat sink block;
X_{SS} thickness of stainless steel region (coolant channel usually);

6.1. Greek symbols

δ_m melt layer thickness;
$\Delta\delta_m$ incremental melt layer thickness;
ε surface emissivity;
ρ material density;
σ Stefan–Boltzmann constant;

6.2. Subscripts

b bulk;
eff effective;
cool coolant;
evap evaporation;
f film;
FDSB fully developed subcooled boiling;
FW first wall;
m melt layer;
OFDSB onset of fully developed subcooled boiling;
ONB onset of nucleate boiling;
PDSB partially developed subcooled boiling;
rad black-body radiation
s surface;
sat saturation;
SP single phase;
w wall;

Acknowledgements

The authors had several useful discussions with Dr H.D. Pacher and Dr I. Smid of the European ITER Home Team, whom they wish to acknowledge also for their technical input and suggestions. They are also grateful to Mrs Birgit Esser for her help with the computer programming and to Dr S. Chiocchio for his review of the manuscript and his helpful suggestions. This paper was prepared as an account of work performed under the Agreement among the European Atomic Energy Community, the Government of Japan, the Government of the Russian Federation, and the Government of the United States of America on Co-operation in the Engineering Design Activities for the International Thermonuclear Experimental Reactor ('ITER EDA Agreement') under the auspices of the International Atomic Energy Agency (IAEA).

References

[1] Technical Basis for the ITER Interim Design Report, Cost Review and Safety Analysis, ITER EDA Documentation Series No. 7 (IAEA, Vienna, 1996).
[2] W.G. Wolfer and A.M. Hassanein, J. Nucl. Mater. 111&112 (1982) 560.
[3] A.M. Hassanein, G.L. Kulcinski and W.G. Wolfer, J. Nucl. Mater. 111&112 (1982) 554.
[4] A.M. Hassanein, G.L. Kulcinski and W.G. Wolfer, Nucl. Eng. Des. Fusion 1 (1984) 307.
[5] A.M. Hassanein, J. Nucl. Mater. 122&123 (1984) 1453.
[6] A. Hassanein and I.I. Konkashbaev, Fusion Eng. Des. 28 (1995) 27.
[7] A. Hassanein, A. Konkashbaev and I. Konkashbaev, in: Proc. 18th Symp. on Fusion Technology, Vol. 1 (1994) p. 223.
[8] J.A. Fillo, Nucl. Eng. Des. 48 (1978) 330.
[9] J.A. Fillo, Nucl. Eng. Des. 68 (1981) 243.
[10] I. Smid, H.D. Pacher, G. Vieider, U. Mszanowski, Yu. Igitkhanov, G. Janeschitz, J. Schlosser and L. Plöchl, in: Proc. 7th Int. Conf. on Fusion Reactor Materials (ICFRM-7), Obninsk, Sept. 1995, J. Nucl. Mater. 233–237 (1996) 701.
[11] ANSYS User's Manual for Revision 5.1, Swanson Analysis Systems, Inc., Houston, PA, USA (Sept. 1994).
[12] G. Federici and A.R. Raffray, this issue, p. 101.
[13] R.A. Langley, J. Bohdansky, W. Eckstein, P. Mioduszewski, J. Roth, E. Taglauer, E.W. Thomas, H. Verbeek and K.L. Wilson, Nucl. Fusion (1984).
[14] M.A. Hoffman, private communication (Mar. 1995).
[15] A.E. Bergles and W.M. Rohsenow, paper 63-HT-22, presented at the Natl. Heat Transfer Conf. of the ASMA-AIChE, Boston, Aug. 11–14, 1963.
[16] P. Saha and N. Zuber, Proc. 5th Int. Heat Transfer Conf., Tokyo, paper B4.7 (1974).
[17] J.G. Collier, Convective Boiling and Condensation, 2nd Ed. (McGraw-Hill, New York, 1982).
[18] J.R.S. Thom et al., paper 6 presented at the Symp. on Boiling Heat Transfer in Steam Generating Units and Heat Exchangers, Manchester, IMechE, Sept. 15–16, 1965.
[19] C. Ibbott, D. Ciric, E. Deksnis, H.D. Falter, A. Peacock and M. Watson, in: Proc. 16th Symp. on Fusion Engineering (SOFE), Champaign–Urbana, ILL, Vol. 1 (Oct. 95) p. 788.
[20] H.D. Falter, D. Ciric, D.J. Godden, C. Ibbott and A. Celentano, J. Nucl. Mater., submitted.
[21] Y. Igitkhanov, H.D. Pacher, G. Federici, G. Janeschitz, D.E. Post and I. Smid, in: Proc. of the Ann. Eur. Phys. Soc. on Controlled Fusion and Plasma Physics – EPS 95, Bournemouth, UK, Vol IV (1995) p. 333.